Cao et al. *NPG Asia Materials* (2018) 10: 670-684
DOI 10.1038/s41427-018-0063-0

NPG Asia Materials

ARTICLE Open Access

Monodisperse Co_9S_8 nanoparticles in situ embedded within N, S-codoped honeycomb-structured porous carbon for bifunctional oxygen electrocatalyst in a rechargeable Zn–air battery

Zhi-qian Cao[1], Ming-zai Wu[1], Hai-bo Hu[1], Guo-jin Liang[2] and Chun-yi Zhi[2]

Abstract

The exploitation of cost-effective, highly active, and robust non-precious metal bifunctional oxygen electrocatalysts for both the oxygen reduction reaction (ORR) and oxygen revolution reaction (OER) is the key to promoting the application of regenerative fuel cells and metal–air batteries. Co_9S_8 is considered a promising non-precious metal bifunctional oxygen electrocatalyst. However, the electrocatalytic performance of cobalt sulfide-based nanocatalysts is still far from satisfactory because of their poor conductivity, insufficient exposed active sites, and aggregation-prone during continuous work. Herein, based on the inspiration from honeycombs in nature, we synthesized Co_9S_8/N, S-codoped honeycomb-structured porous carbon (Co_9S_8/NSC) in situ composites via a simple method. Benefiting from the unique honeycomb composite structure composed of monodisperse Co_9S_8 nanoparticles in situ embedded within the three-dimensional interconnected network carbon matrix with high conductivity, which facilitates not only the electron transport and charge transfer across the interface but also the exposure of active sites and rapid transport of ORR/OER-related species, the obtained Co_9S_8/NSC in situ composites exhibit high stability and activity in both the ORR in terms of more a positive half-wave potential (0.88 V vs. RHE) than that (0.86 V vs. RHE) of commercial 20% Pt/C and the OER in terms of a small overpotential (0.41 V vs. RHE) approaching that of commercial IrO_2 (0.39 V vs. RHE) in alkaline electrolytes at 10 mA cm^{-2}. Thus, as expected, the assembled rechargeable Zn–air batteries based on the bifunctional electrocatalysts exhibit a small discharge/charge overpotential (0.96 V) with a high voltaic efficiency of 55.1% at 10 mA cm^{-2} and a long-term cycling stability of over 4000 min.

Introduction

With the gradual exhaustion of non-renewable resources, such as fossil fuels, and the increasing seriousness of environmental pollution, finding alternative energy sources has been a global concern. To solve this urgent problem, many attempts and painstaking experiments have been done to explore variously alternative energy storage and conversion technologies, such as solar power batteries, lithium-ion batteries, supercapacitors, fuel cells (FCs), metal–air batteries, etc. Among them, FCs and metal–air batteries, by virtue of the obvious advantages, such as low cost, resource abundant, eco-friendly, good safety, and high-energy density, are considered a promising solution for clean and sustainable energy generation[1–4]. However, the indispensable catalysts, especially those with bifunctional catalytic activity for both the oxygen reduction reaction (ORR) and the oxygen

Correspondence: Ming-zai Wu (wumz@ustc.edu.cn) or Hai-bo Hu (haibohu@ahu.edu.cn) or Chun-yi Zhi (cy.zhi@cityu.edu.hk)
[1]School of Physics and Materials Science, Anhui University, Hefei, China
[2]Department of Physics and Materials Science, City University of Hong Kong, 83 Dachi Road, Kowloon, Hong Kong SAR, China

revolution reaction (OER) in regenerative FCs and metal-air batteries, have remained a technological bottleneck for their large-scale commercialization[5–7]. Traditionally, platinum (Pt) and Pt-based materials are considered the most effective electrocatalysts for the ORR. However, they usually suffer issues of high cost, scarcity, and poor stability[8–11]. On the other hand, ruthenium or iridium oxides (RuO_2 or IrO_2) exhibit excellent OER catalytic behavior but relatively poor ORR activity[12,13]. Therefore, it is still a great challenge to prepare low-cost, resource-rich, and robust bifunctional oxygen electrocatalysts with both high OER and ORR catalytic activity for applications in highly efficient regenerative FCs and metal–air batteries to promote their practical applications.

Recently, noticeable progress has been made in the development of low-cost, resource-rich, and highly efficient oxygen catalysts for the ORR and OER to replace traditional precious metals[14–20]. Notably, both theoretical calculations and experimental results indicate that monodisperse Co_9S_8 nanocatalysts can serve as highly efficient bifunctional oxygen electrocatalysts for both the ORR and OER[21–23]. However, the electrocatalytic performance of cobalt sulfide-based nanocatalysts is still far from satisfactory because they show poor conductivity, have insufficient exposed active sites and are prone to aggregation during continuous work[24–26]. Therefore, determining how to effectively increase the catalytic active sites, enhance the electrical conductivity of electrocatalysts, and inhibit the aggregation of monodisperse Co_9S_8 nanocatalysts during continuous work is critical for the exploitation of their potential catalytic activities. Carbon materials, by virtue of their excellent conductivity and high specific surface area, are considered to be an ideal carrier for monodisperse nanocatalysts, such as Co_9S_8 to improve their poor electrical conductivity and inhibit aggregation. More interestingly, doping of carbon materials with highly electronegative heteroatoms, such as nitrogen can further significantly increase their conductivity by providing an advantageous channel for electron mobility[27–30]. In addition, doping with nitrogen heteroatoms will provide a strong polarization in the carbon matrix, resulting in an improved binding capacity of adjacent carbon to molecular oxygen and then enhanced ORR and OER activities[31–33]. In addition, the electronegativity of sulfur, close to carbon, is considered to be able to increase the exposed edge positions and disordered sites in carbon materials, such as graphene, which can enhance the electrochemical activity, stability, and alcohol resistance of carbon materials in alkaline medium[34–38]. Therefore, to fully explore the potential catalytic activities of Co_9S_8 electrocatalysts in both the ORR and OER, a combination of monodisperse Co_9S_8 nanocatalysts with heteroatom-doped carbon carrier becomes appealing to improve the poor conductivity, expose more active sites, and obtain an enhanced synergistic catalytic effect.

In this work, based on the inspiration from honeycombs in nature, we fabricated N, S-codoped honeycomb-structured porous carbon with in situ embedded monodisperse Co_9S_8 nanoparticles (2–20 nm) for highly efficient bifunctional supported electrocatalysts in Zn–air batteries. The unique honeycomb-structured porous composite structure design has multiple advantages. First, the formation of a highly conductive N, S-codoped carbon matrix synchronously accompanied by the generation of monodisperse in situ embedded Co_9S_8 nanoparticles gives the obtained Co_9S_8 nanocatalysts improved conductivity and good stability during continuous work. Second, the three-dimensional (3D) interconnected porous network with high specific surface area is propitious to loading monodisperse Co_9S_8 nanoparticles, providing more active sites accessible to the electrolyte. Last but not the least, the 3D interconnected porous network is also beneficial for the mass transport of electrolyte ions and ORR/OER-related species during the catalytic process, allowing a rapid and sustained reaction. As expected, benefiting from the reasonable structural design and appropriate materials selection, the as-fabricated Co_9S_8/N, S-codoped honeycomb-structured porous carbon (Co_9S_8/NSC) in situ composites exhibit not only excellent ORR catalytic activity, of which the half-wave (0.88 V vs. RHE) potentials clearly outperformed that of the commercial 20% Pt/C (0.86 V vs. RHE) but also good catalytic activity and stability for the OER in terms of a small overpotential (0.41 V vs. RHE at 10 mA cm^{-2}) approaching that of commercial IrO_2 (0.39 V vs. RHE) in alkaline electrolytes. Thus, as a proof-of-concept application, the further assembled rechargeable Zn–air batteries based on the bifunctional electrocatalysts exhibit a small discharge/charge overpotential (0.96 V) with a high voltaic efficiency of 55.1% at 10 mA cm^{-2} and a long-term cycling stability over 4000 min.

Experimental procedures

Synthesis of SiO_2 nanospheres

SiO_2 nanoparticles were prepared by the Stöber method[39]. In a typical procedure, 4.5 mL of tetraethyl orthosilicate was added to a mixed solution containing 65.0 mL of ethanol and 25.0 mL of deionized (DI) water under vigorous stirring. Then, 9 mL of aqueous ammonia solution was added dropwise to the above mixture. The mixture was stirred for 8 h at room temperature. Subsequently, the product was centrifuged and washed several times with ethanol and DI water. Finally, the white SiO_2 nanospheres with an average size of ~200 nm were obtained after drying overnight at 60 °C.

Preparation of honeycomb-structured porous Co_9S_8/NSC in situ composite electrocatalyst

First, 0.1 g of $Co(NO_3)_2{\cdot}6H_2O$ was dissolved in 50 mL of alcohol solution (37.5% ethanol) to form a red solution. Then, 1.0 g of SiO_2 nanospheres, 1.0 g of thiourea ($CS(NH_2)_2$), and 0.5 g of glucose were successively added to the above solution under continuous stirring at room temperature for 2 h. Then, the as-obtained mud-like precursor was placed in tube furnace and heated to 900 °C for 2 h in a N_2 atmosphere. After further natural cooling, the sample was immersed in 2 M NaOH solution at 50 °C for 8 h to remove the SiO_2 template, and then centrifuged and washed with DI water to remove residual NaOH until reaching pH = 7. Finally, the honeycomb-structured porous in situ composites, i.e., Co_9S_8/NSC-900 porous composites, were obtained after drying overnight at 60 °C. For comparison, a series of catalysts labeled C-900, NSC-900, Co_9S_8/NSC-800, and Co_9S_8/NSC-1000 were also prepared using similar procedures, but without ($CS(NH_2)_2$), without $Co(NO_3)_2{\cdot}6H_2O$, and at 800 and 1000 °C, respectively.

Characterization

The microstructure and phase composition of the as obtained samples were characterized by X-ray powder diffraction (XRD Bruker D8-ADVANCE) with an 18 kW advanced X-ray diffractometer with Cu K_α radiation (λ = 1.54056 Å), Raman spectroscopy (inVia-Reflex, Renishaw, UK), an elemental analyzer (EA, Perkin-Elmer 2400 CHN), field-emission scanning electron microscopy (FE-SEM, S-4800, Hitachi, Japan), transmission electron microscopy (TEM, JEM-2100, JEOL, Japan), and Fourier transform infrared spectroscopy (VERTEX 801HYPERION2000, Bruker Optics, Germany). The surface area was determined by a nitrogen adsorption–desorption method at 77 K (3H-2000PS2, BeiShiDe Instrument, China). X-ray photoelectron spectroscopy (XPS) was conducted with a Mg Kα achromatic X-ray source. Thermo-gravimetric analysis (TGA) measurements were performed on Diamond TG 6300 at a heating rate of 10 C min^{-1} in an air atmosphere in the range of 40–900 °C. The surface areas and pore sizes of the as-prepared samples were analyzed by the nitrogen adsorption–desorption isotherms (BET, Quantachrome, NOVAe). Inductively coupled plasma-atomic emission spectrometry (ICP-AES) measurements were conducted to determine the cobalt and sulfur concentrations of the samples with an Optima 7400 DV instrument.

Electrochemical measurements

All the ORR tests were performed on the electrochemical work station (CHI 660E, Chenhua, Shang-hai) in a conventional three-electrode cell equipped with a Pt wire counter electrode, an Ag/AgCl reference electrode and a glassy carbon (GC) disk electrode. The measured potentials are referred to the RHE, $E_{RHE} = E_{Ag/AgCl} + 0.059\,pH + E^{\theta}_{Ag/AgCl}$. The rotating disk electrode (RDE) was used as the working electrode. For each sample, 5 mg of catalysts were ultrasonically dispersed in a suspension containing 700 μL of DI water, 300 μL of isopropanol and 50 μL of 5 wt% Nafion solution. Subsequently, the obtained homogeneous catalyst ink with a volume of 8 μL was dripped on a GC RDE (5 mm in diameter) and dried thoroughly at room temperature. The Pt/C catalyst (20 wt %) ink was prepared as described above for comparison. In alkaline media, the RDE test was carried out at room temperature in O_2-saturated 0.1 M KOH solution. The cyclic voltammetry (CV) measurements were scanned from −0.9 to 0.1 V (vs. Ag/AgCl) at a scan rate of 20 mV s^{-1}. The RDE test was carried out by linear sweep voltammetry (LSV) at a potential range of −0.9 to 0.2 V (vs. Ag/AgCl) at a scanning rate of 5 mV s^{-1} at different rotational rates of O_2-saturation at 400–2500 rpm alkaline electrolyte. Under the same conditions, OER measurements were carried out by LSV at a potential range from 0 to 1.0 V (vs. Ag/AgCl) at a scanning rate of 5 mV s^{-1} under 1600 rpm. The IrO_2 catalyst ink was prepared as described above for comparison. Koutecky–Levich (K–L) plots were obtained from the ORR polarization curves at different potentials. The electron transfer number (n) per O_2 molecule in the ORR was determined by the slopes of the linear fit lines on the basis of the following K–L equation:

$$\frac{1}{j} = \frac{1}{j_k} + \frac{1}{B\times\omega^{1/2}} \quad (1)$$

$$B = 0.2\times n\times F\times C_{O_2}\times D_{O_2}^{\frac{2}{3}}\times \nu^{-\frac{1}{6}} \quad (2)$$

where j is the measured current density, j_k is the kinetic current density, ω is the electrode rotation rate, F is the Faradic constant (96,485 C mol^{-1}), C_{O2} is the saturated oxygen concentration in 0.1 M KOH aqueous solution (1.2×10^{-6} mol cm^{-3}), D_{O2} is the oxygen diffusion coefficient (1.73×10^{-5} cm^2 s^{-1}), ν is the kinematic viscosity of the solution (0.01 cm^2 s^{-1}) and n is the electron transfer number in the ORR. Rotating ring-disk electrode (RRDE) voltammogram measurements for the calculation of the ORR electron transfer number were conducted on an RRDE configuration with a 320 μm gap Pt ring electrode. The electron transfer numbers (n) and peroxide yield (HO_2^-%) can be obtained from the RRDE curve using Eqs. (3) and (4), respectively.[40]

$$n = 4\times\frac{I_d}{I_d + I_r/N} \quad (3)$$

$$HO_2^-\% = 200\frac{I_r/N}{I_d + I_r/N} \quad (4)$$

where I_d is the disk current, I_r is the ring current and N is the current collection efficiency of the Pt ring which was determined to be 0.37.

Fabrication and test of Zn–air batteries

The Zn–air battery test was conducted in a homemade battery, with a Zn plate serving as the anode and catalyst-coated carbon cloth (1 cm^2) serving as the air electrode. Typically, 5 mg of catalysts were ultrasonically dispersed into 1 mL of ethanol and 50 μL of Nafion solution by sonication for 30 min. Then, some amount of the catalyst ink was dropped on the carbon paper to obtain a catalyst loading of 1 mg cm^{-2}. The electrolyte was a 6 M KOH solution containing 0.2 M $Zn(Ac)_2$. Battery tests were carried out an electrochemical workstation at room temperature.

Results and discussion

Characterizations of Co_9S_8/NSC in situ composites

The detailed preparation process for the Co_9S_8/NSC in situ composites is schematically illustrated in Fig. 1. The easily manipulated synthesis protocol first began with mixing SiO_2 nanospheres, thiourea, and glucose with Co $(NO_3)_2{\cdot}6H_2O$ solution. Then, the obtained precursor was thermally treated, during which glucose was pyrolyzed into the N, S-codoped carbon matrix with the in situ formed monodisperse Co_9S_8 nanoparticles (2–20 nm) and encapsulated SiO_2 nanospheres. Finally, the encapsulated SiO_2 nanospheres templates were removed by being dissolved in 2 M NaOH solution and washed away by DI water. Thus, the Co_9S_8/NSC in situ composites were obtained. It should be noted that the easily manipulated synthesis method does not involve tedious operations and any expensive equipment or reagents, which is beneficial for the scale-production of the low-cost catalysts and their commercial application.

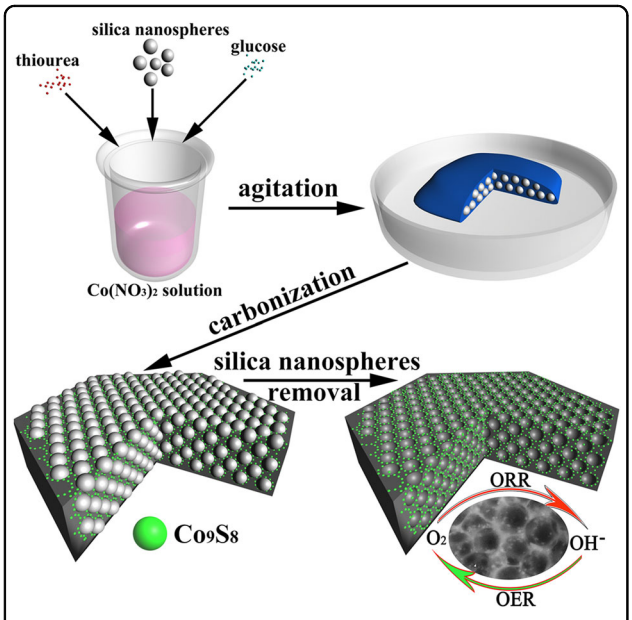

Fig. 1 Flowchart of the easily-manipulated synthesis protocol for the Co_9S_8/N, S-codoped honeycomb-structured porous carbon in-situ composites

X-ray diffraction (XRD) was first used to determine the crystalline phase of the synthesized samples. Figure 2a shows the XRD patterns of the Co_9S_8/NSC-900 product, and the contrast samples C-900 and NSC-900. As shown, the diffraction peaks at $2\theta = 15.8°$, 29.8°, 31.2°, 39.5°, 47.6°, and 51.9° are ascribable to the (111), (311), (222), (331), (511), and (440) planes, respectively, of Co_9S_8 (JCPDS card 65-6801)[23,41,42], directly indicating the successful of formation of Co_9S_8 within the porous carbon skeleton. In addition, the energy-dispersive spectrum (EDS) (Figure S1a) also shows the contained Co, N, S, C, and O elements in the Co_9S_8/NSC-900 product. A representative Raman spectrum of the as-obtained Co_9S_8/NSC-900 is further shown in Fig. 2b, which can be divided into two parts: <800 and >800 cm^{-1}. The Raman bands below 800 cm^{-1} can be indexed to Co_9S_8, and those above 800 cm^{-1} are related to amorphous carbon in the Co_9S_8/NSC-900 composite. Typical D and G bands of amorphous carbon located at 1369 and 1583 cm^{-1} were clearly observed in this spectrum, indicating the formation of carbonaceous composites after pyrolysis. The relative intensity ratio of the D band to the G band (I_D/I_G) has been widely adopted for evaluating the graphitization degree of carbon[43,44]. The I_D/I_G ratios of NSC-900 (0.95) and Co_9S_8/NSC-900 (0.94) are lower than that of C-900 (1.03), which can be attributed to the N and S heteroatom doping. The results show that N and S heteroatom doping causes many defects in the internal portion of honeycomb-like porous carbon skeleton, which can further enhance the degree of graphite, resulted in improved catalyst conductivity and catalytic activity.

To investigate the porosity of C-900, NSC-900, and Co_9S_8/NSC-900 samples, nitrogen adsorption–desorption isotherms were further measured. As shown in Fig. 2c, all the samples display a type-IV curve with a distinct hysteresis loop, indicating the presence of many mesopores and macropores in these samples[45]. The specific surface area of the Co_9S_8/NSC-900 is determined to be 556 m^2 g^{-1}, which is clearly larger than that of the C-900 (417 m^2 g^{-1}) and NSC-900 (490 m^2 g^{-1}). According to the Barrett–Joyner–Halenda (BJH) method, these samples mainly contain mesopores with diameters between 2 and 20 nm (Fig. 2d). The nonlocal density functional theory (NLDFT) method was further employed to analyze the pore size distribution of Co_9S_8/NSC-900 in situ composites more rigorously. As clearly shown in Figure S1b, in addition to the mesopores with diameters between 2 and 20 nm, the Co_9S_8/NSC-900 in situ composites also contain a large number of micropores with diameters between 0.89 and 2.0 nm. We think that these micropores and mesopores are mainly derived from the combined action of the

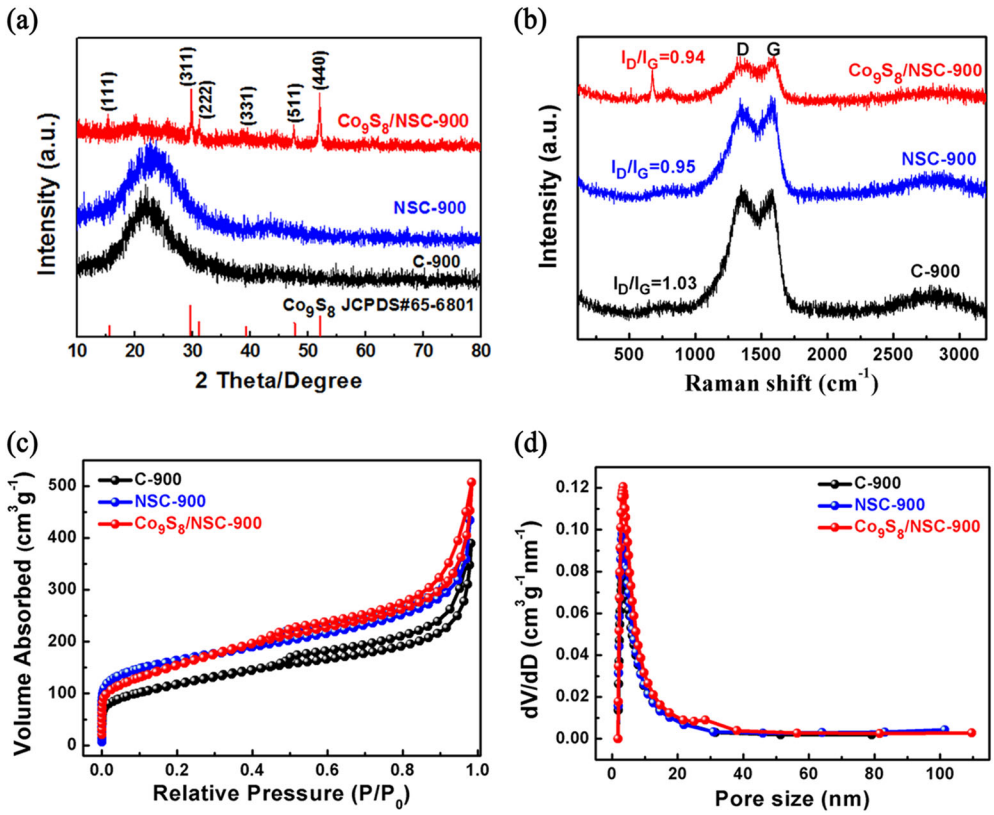

Fig. 2 Characterization of composition and pore size distribution of the samples, **a** XRD patterns of C-900, NSC-900 and Co_9S_8/NSC-900; **b** Raman spectra of C-900, NSC-900 and Co_9S_8/NSC-900; **c** N2 adsorption-desorption isotherms, and **d** BJH pore-size distribution of C-900, NSC-900 and Co_9S_8/NSC-900

released gases in the annealing process and following alkaline etching process, resulting in a large specific area of the as-prepared the Co_9S_8/NSC-900 in situ composites with a honeycomb-like porous structure. This is of great significance for catalytic applications, as it can effectively facilitate the exposure of active sites and rapid transport of ORR/OER-related species, allowing a rapid and sustained reaction.

Figure 3a shows a typical SEM image of the SiO_2 nanospheres used in the synthesis with a uniform average diameter of ~200 nm. By taking advantage of the SiO_2 nanosphere template, the as-obtained NSC-900, Co_9S_8/NSC-800, Co_9S_8/NSC-900, and Co_9S_8/NSC-1000 products have a similar honeycomb-like porous structure, as clearly demonstrated in the SEM image (Fig. 3b–d and Figure S1c–d). The typical optical photo of a natural honeycomb in the inset of Fig. 3b clearly shows a high degree of structural similarity to the as-obtained samples. As further shown in the enlarged SEM image (Fig. 3e), the prepared honeycomb-structured porous Co_9S_8/NSC-900 composites consist of a number of interconnected macropores composed of carbon film with high conductivity, whose surface is uniformly covered with in situ generated and embedded monodisperse Co_9S_8 nanoparticles with diameters from 2 to 20 nm. The joint action of the dissolution of SiO_2, the surface tension, as well as the mild chemical reaction promotes the formation of the honeycomb-like structure. We further carried out EDS-mapping analysis of the Co_9S_8/NSC-900 sample. As shown in Fig. 3f–i, the uniform dispersion of C, N, S, and Co elements across the entire image directly indicates the formation of Co_9S_8/NSC in situ composites.

The morphology and microstructure of the Co_9S_8/NSC-900 in situ composites were further characterized with TEM and high-resolution TEM (HRTEM). As clearly shown in Fig. 4a, b, the Co_9S_8/NSC-900 in situ composites have a unique honeycomb-like porous hybrid structure composed of a large number of in situ generated monodisperse Co_9S_8 nanoparticles uniformly dispersed on the carbon skeleton with high conductivity. Figure 4c, d are the HRTEM images of the monodisperse Co_9S_8 nanoparticles with obvious lattice edges. The measured lattice distance of 0.29 nm corresponds to the (311) plane of Co_9S_8. Notably, as shown in Fig. 4c, d, the in situ generated Co_9S_8 nanoparticles (2–20 nm) were tightly encapsulated by the carbon film. The unique in situ embedding

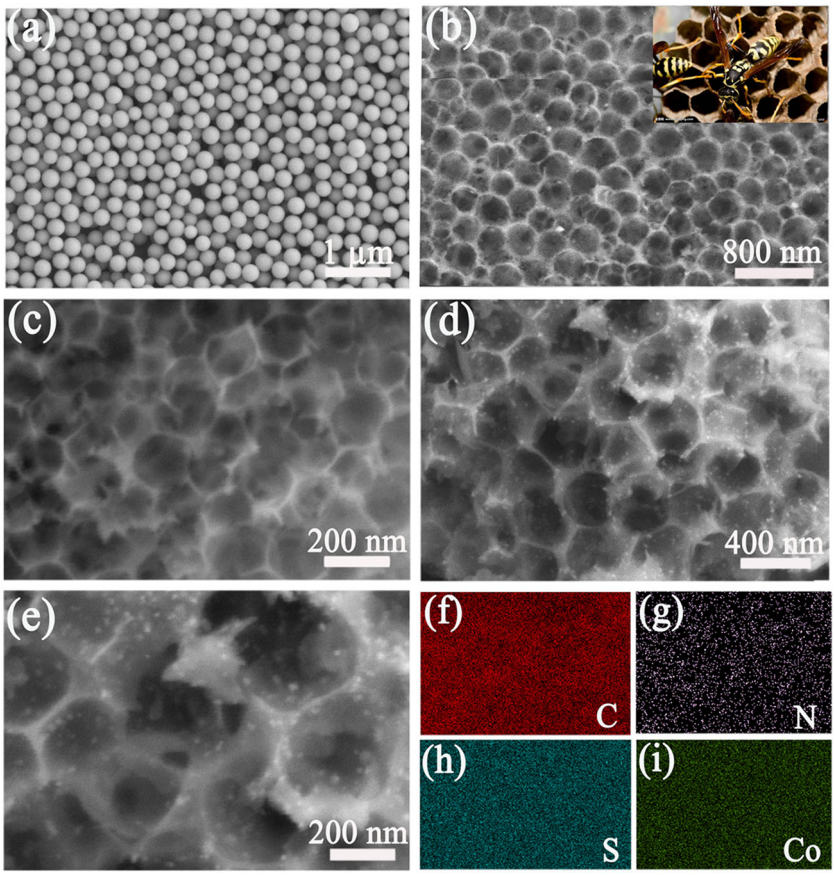

Fig. 3 Typical SEM images of the smaples, **a** SiO_2 nanospheres; **b**, **c** NSC-900; **d**, **e** Co_9S_8/NSC-900, and corresponding C, N, S, and Co elemental mapping **f**-**i** of the prepared Co_9S_8/NSC-900 in-situ composites. The inset in **b** is a typical optical photo of natural honeycomb for contrast

configuration would greatly reduce the tendency of agglomeration of monodisperse Co_9S_8 nanoparticles and simultaneously improve their poor conductivity, resulting in enhanced ORR/OER catalytic activity. The electron diffraction rings shown in the inset of Fig. 4d further indicate the porous honeycomb structure of the Co_9S_8/NSC-900. Two typical partial diffraction rings were indexed in the SAED pattern and can be assigned to the (311) and (440) planes of the Co_9S_8 phase. All the above results fully proved the successful fabrication of honeycomb-structured porous Co_9S_8/NSC-900 in situ composites, which could be expected to exhibit excellent ORR/OER catalytic activity depending on the produced graphitic carbon skeleton with high conductivity, codoped pyridinic-N and thiophene-S heteroatoms, and the in situ embedded monodisperse Co_9S_8 nanoparticles.

To shed light on the chemical compositions and elemental valence states of the Co_9S_8/NSC-900 in situ composites, XPS, elemental analysis (EA), thermogravimetric analysis (TGA), and ICP-AES measurements were further carried out. Figure 5a is the XPS survey spectrum, which indicates the presence of C, N, S, and Co. The resulting estimated atomic weight percentages are 84.29% for C, 8.27% for N, 3.59% for S, and 3.85% for Co, respectively, which reveals that the atomic ratio of S:Co is approximately 1:1.07, consistent with the atomic ratio of S:Co in the chemical molecular formula of Co_9S_8. In addition, the atomic ratio is also congruent with that calculated from the EDS-mapping analysis (Table S1). These results forcefully prove the formation of cobalt sulfides in the composite. A typical TGA curve (Figure S2a) illustrates the weight loss of the as-prepared Co_9S_8/NSC-900 sample with the temperature increase from 40 to 900 °C in air. The sample has an initial loss of weight (~18 wt%) below 400 °C, which can be ascribed to the removal of absorbed water and air because of the large specific surface area of the as-prepared Co_9S_8/NSC-900 sample. However, there is a significant weight drop in the temperature range from 400 to 500 °C, mainly attributed to the loss of carbon. The final remnant product (17.08 wt%) is mainly Co_3O_4 transformed from Co_9S_8 during the thermogravimetric process in the air, which can be proven from the obtained XRD pattern of the final remnant product, as shown in Figure S2b. It is

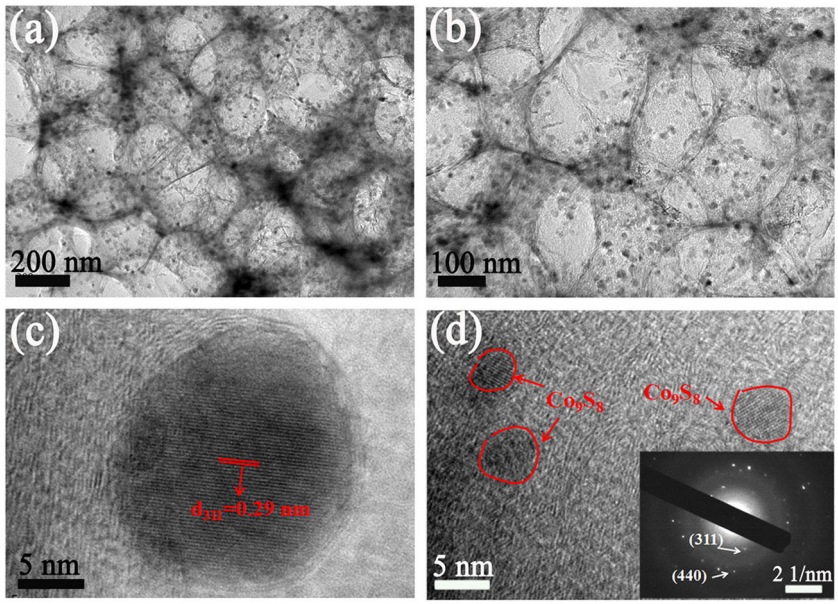

Fig. 4 Typical TEM images of the samples, **a**, **b** Co_9S_8/NSC-900 in-situ composites; and **c**, **d** the corresponding HRTEM image and electron diffraction pattern image of Co_9S_8/NSC-900 in-situ composites

worth noting that no diffraction peaks belonging to silicon dioxide are observed in the XRD pattern, which indicates that the as-prepared Co_9S_8/NSC-900 sample has a very low level of unremoved silicon dioxide. According to the EA and ICP-AES results for Co_9S_8/NSC-900, the estimated weight percentages of C, N, S, and Co, are approximately 53.87, 5.74, 7.44, and 15.03 wt%, respectively (Table S1). The weight percentage of the missing element is also consistent with the results from TGA. Detailed information about the bonding configuration of each element was further given by high-resolution XPS spectra; the schematic of different types of nitrogen and sulfur is shown in Fig. 5b. The high-resolution spectrum of C 1s (Fig. 5c) can be deconvoluted into several peaks, corresponding to C = C–C (284.5 eV), C–S–C (285.4 eV), C–N–C (286.5 eV), and C = O (288.4 eV), indicating that N and S were successfully doped into the carbon skeleton[29,46,47]. For the high-resolution N 1s XPS spectrum (Fig. 5d), the N 1s peak can also be deconvoluted into three peaks, corresponding to pyridinic N (398.6 eV), pyrrolic N (400.2 eV), and graphitic N (401.4 eV), indicating N doping in the graphitic carbon structure[48–50]. Figure 5e shows the high-resolution S 2p XPS spectrum for the Co_9S_8/NSC-900 in situ composites. In the S 2p XPS spectrum, the raw curve can be peak-fitted into four curves attributed to three different types of sulfur species. The peaks at 161.6 and 163.5 eV can be assigned to the S $2p_{3/2}$ and S $2p_{1/2}$ binding energies of S^{2-} in Co_9S_8, respectively, and the peaks at 164.6 and 168.1 eV are attributed to C–S and SO_4^{2-}, respectively. The presence of C–S may originate from the interfaces between Co_9S_8 and the carbon matrix, whereas SO_4^{2-} arose from partly oxidized sulfur species or residual sulfate groups on the surface of the material. In the Co 2p spectrum of the Co_9S_8/NSC-900 (Fig. 5f) in situ composites, the peaks at 796.68 and 798.54 eV are, respectively, assigned to the $2p_{1/2}$ of Co^{2+} and Co^{3+}, and the peaks at 781.03 and 783.18 eV, respectively, belong to the $2p_{3/2}$ of Co^{2+} and Co^{3+}[51,52], as well as the corresponding two shakeup satellites peaks (abbreviated as "Sat."), also suggesting the formation of cobalt sulfides in the carbon structure.

As is well-known, temperature is an important parameter that affects the structure and composition of the prepared catalyst, thus determining the ORR activities. Therefore, the Co_9S_8/NSC catalysts prepared at lower temperature (800 °C) and higher temperature (1000 °C) were further studied to determine the best heat treatment conditions. The crystalline structures of the as-obtained Co_9S_8/NSC-800 and Co_9S_8/NSC-1000 were first characterized by X-ray diffraction (XRD). As Figure S2c shows, all the corresponding XRD diffraction patterns confirm the successful formation of Co_9S_8 in the 3D porous carbon skeleton at both lower or higher pyrolysis temperatures. However, it is worth noting that, as the pyrolysis temperature increases, the peak intensity of N 1s and S 2p gradually reduced, indicating that the contents of doped N and S decreased, as shown in Figure S2d. Even so, as further clearly shown in the high-resolution N 1s and S 2p spectra (Figure S3a–h), the relative percentages of pyrrolopyridine-N and pyridine-N decreased with the

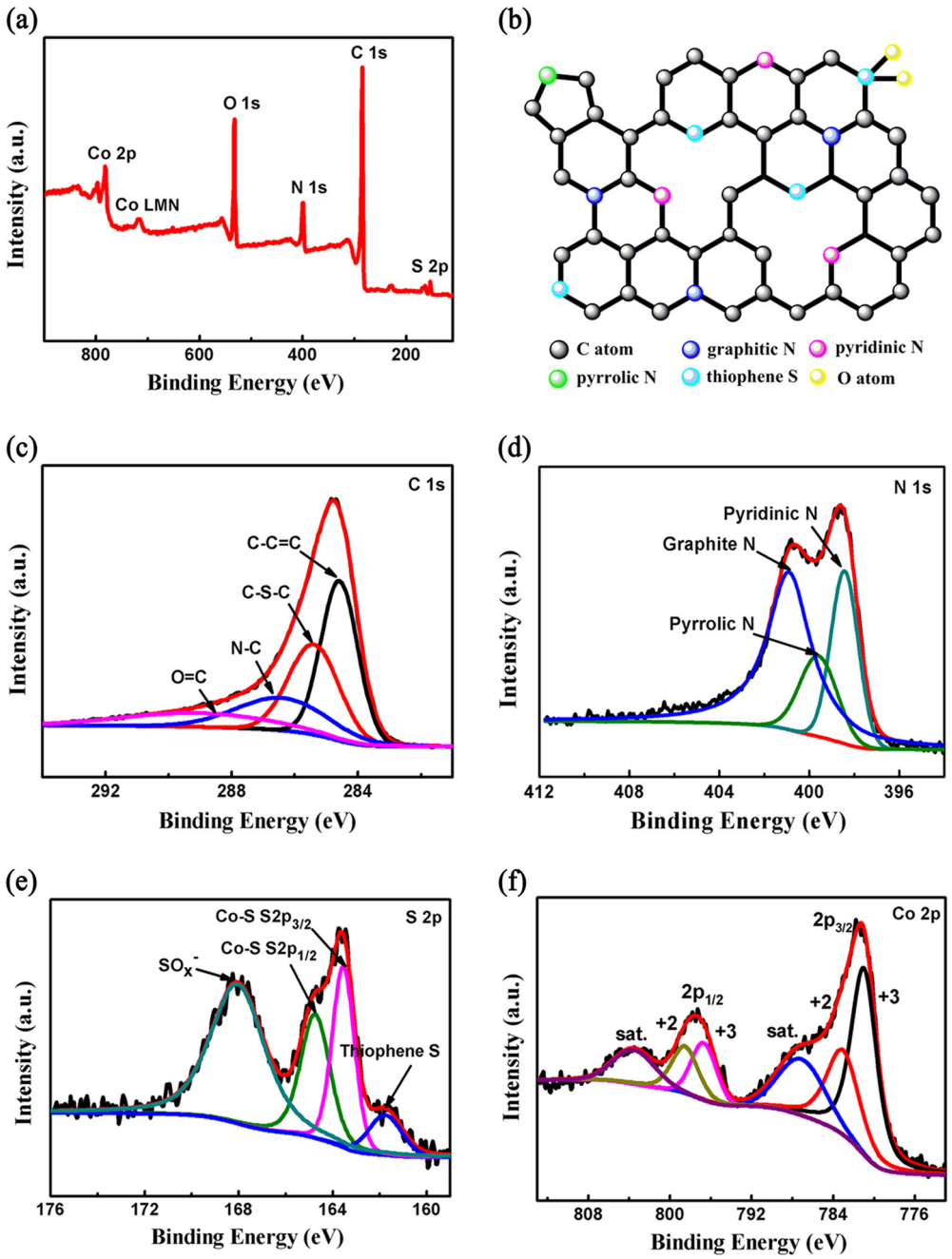

Fig. 5 XPS survey spectrum of the samples, **a** Co_9S_8/NSC-900 in-situ composites; **b** schematic of 10.1038/s41427-018-0063-0 different types of nitrogen and sulfur in Co_9S_8/NSC-900 in-situ composites; **c-f** high-resolution spectra of C 1s, N 1s S 2p and Co 2p for Co_9S_8/NSC-900 in-situ composites, respectively

increase in pyrolysis temperature, while the relative percentage of graphite-N and thiophene-S increased and the intensity of Co–S bonds became gradually higher. These results indicate that higher pyrolysis temperature favors the conversion of doped-N from pyrrolopyridine-N/pyridinic-N to graphitic-N and doped-S from SO_x to thiophene-S. The graphitic-N groups have been demonstrated to be the active species for the ORR/OER[53–57]. In addition, thiophene-S is considered to be able to increase the exposed edge positions and disordered sites in carbon materials, such as graphene, which can enhance the electrochemical activity, stability, and alcohol resistance of carbon materials in alkaline media[34–38]. Electrochemical impedance spectrum (EIS) measurements were further carried out to investigate the potential impact of pyrolysis temperature on the catalytic performance of the

as-obtained samples. As shown in Figure S3i, with the increase in the pyrolysis temperature, the as-obtained samples tend to show a lower charge-transfer resistance (Rct, 22.3 Ω for Co_9S_8/NSC-800, 8.4 for Co_9S_8/NSC-900, and 14.2 Ω for Co_9S_8/NSC-1000), which can be attributed to the enhanced conductivity of the 3D porous carbon matrix with increased graphitic-N and thiophene-S content, facilitating the electron transport across the interfaces between the Co_9S_8, carbon skeleton, and electrolyte. This is also very beneficial for the improvement of the catalytic activity of the prepared catalyst. Thus, based on the above characterization results, under the combined action of the higher proportion of graphite-N, thiophene-S, the in situ embedded active Co_9S_8 nanocatalysts, as well as the unique honeycomb porous carbon skeleton with enhanced conductivity, the Co_9S_8/NSC-900 composite catalysts could be expected to exhibit better catalytic activity and electrochemical kinetics compared to those of the other two samples.

Electrochemical performance for ORR and OER

The electrochemical ORR activity properties of the Co_9S_8/NSC-900 in situ composites and all the additional samples in O_2 or N_2-saturated 0.1 M KOH were first evaluated through CV measurements (Fig. 6a). Generally, higher peak potential and larger peak current mean higher catalytic activity. It is obvious that both the peak potential and peak current of honeycomb-like Co_9S_8/NSC-900 in situ composites are larger than those of C-900 (peak potential at 0.78 V vs. RHE) and the NSC-900 (peak potential at 0.84 V vs. RHE), indicating better ORR activity with a higher peak potential at 0.88 V (vs. RHE). To gain better insight into the kinetics of the ORR catalyzed by Co_9S_8/NSC-900, linear sweep voltammograms (LSVs) were also collected in O_2-saturated 0.1 M KOH at an electrode rotation rate of 1600 rpm. Figure 6b and Figure S4 show that the Co_9S_8/NSC-900 in situ composites show an onset potential of 0.96 V (vs. RHE), approaching the value of the commercial 20% Pt/C (1.0 V vs. RHE). Meanwhile, the Co_9S_8/NSC-900 in situ composites exhibit a more positive half-wave potential (0.88 V vs. RHE) than that of C-900 (0.78 V vs. RHE), NSC-900 (0.84 V vs. RHE), Co_9S_8/NSC-800 (0.85 V vs. RHE), Co_9S_8/NSC-1000 (0.85 V vs. RHE), and the commercial 20% Pt/C (0.86 V vs. RHE), respectively. The current density (at 0.2 V vs. RHE) of the Co_9S_8/NSC-900 in situ composites (5.56 mA cm^{-2}) was also higher than those found for C-900 (3.45 mA cm^{-2}), NSC-900 (3.84 mA cm^{-2}), Co_9S_8/NSC-800 (4.75 mA cm^{-2}), Co_9S_8/NSC-1000 (5.18 mA cm^{-2}), and the commercial 20% Pt/C (5.51 mA cm^{-2} V). To further evaluate the structural and compositional advantages of Co_9S_8/NSC-900, the Tafel plots of the Co_9S_8/NSC-900 and contrastive samples, derived from the ORR polarization curves, are shown in Fig. 6c. The corresponding Tafel slopes of Co_9S_8/NSC-900, Co_9S_8/NSC-1000, Co_9S_8/NSC-800, and 20% Pt/C were calculated to be 64, 66, 69, and 72 mV dec^{-1}, respectively. The smaller Tafel slope indicates a superior ORR activity of Co_9S_8/NSC-900. All of the above results fully indicate the better ORR activity of honeycomb-like Co_9S_8/NSC-900 in situ composites compared to that of commercial 20% Pt/C and the additional samples in the study.

LSVs were recorded at different rotation rates (Fig. 6d) to further investigate the ORR kinetics of the Co_9S_8/NSC-900 in situ composites. The K–L plots (Fig. 6d, inset) show a good linear relationship for the Co_9S_8/NSC-900 in situ composites and the measured electron transfer number is close to 4, suggesting that the ORR on the Co_9S_8/NSC-900 catalyst mainly follows the effective four-electron pathway, in which the oxygen molecule (O_2) is reduced to OH^- directly. In addition, to quantify the yield of the peroxide intermediate, as well as the electron transfer number, RRDE measurements with superior precision were further carried out (Fig. 6e). Based on the ring current and disk current, the average electron-transfer number (n) of Co_9S_8/NSC-900 is calculated to be 3.98 in the potential range from 0.8 to 0.2 V with a low H_2O_2 yield of 3.4% (Fig. 6e, inset), which is close to those of 20% Pt/C (H_2O_2 yield of 2.96%, n of 3.99, Figure S5a and b). This effectively indicates that the ORR process under the action of the Co_9S_8/NSC-900 catalyst was almost the four-electron pathway in the alkaline electrolyte, which can be depicted as follows:

$$O_2 + 2H_2O + 4e^- \rightarrow 4OH^-$$

The durability and tolerance to the methanol poisoning effect of the Co_9S_8/NSC-900 in situ composites and commercial 20% Pt/C in O_2-saturated 0.1 M KOH solution (Figure S5c–f) are also evaluated through the LSV curves, respectively. Notably, the LSV curve of the Co_9S_8/NSC-900 in situ composites did not change significantly (Figure S5c) when 0.5 M CH_3OH was added to the O_2-saturated 0.1 M KOH solution. In sharp contrast, the commercial 20% Pt/C catalyst underwent tremendous changes (Figure S5d). The results suggested that the Co_9S_8/NSC-900 catalyst has superior resistance to methanol poisoning than the commercial 20% Pt/C catalyst. In addition, the respective cycling stability of the Co_9S_8/NSC-900 in situ composites and the commercial 20% Pt/C was also evaluated by cycling the catalyst between 0.2 and 1.1 V (vs. RHE) at a high scan rate of 300 mV s^{-1} in O_2-saturated 0.1 M KOH. The current density observed in the LSV curve of the Co_9S_8/NSC-900 recorded after the 10,000 cycles decreased a little compared to that observed in the initial LSV curve (Figure S5e). In comparison, the commercial 20% Pt/C exhibited an obvious current density decay only after 2000 cycles

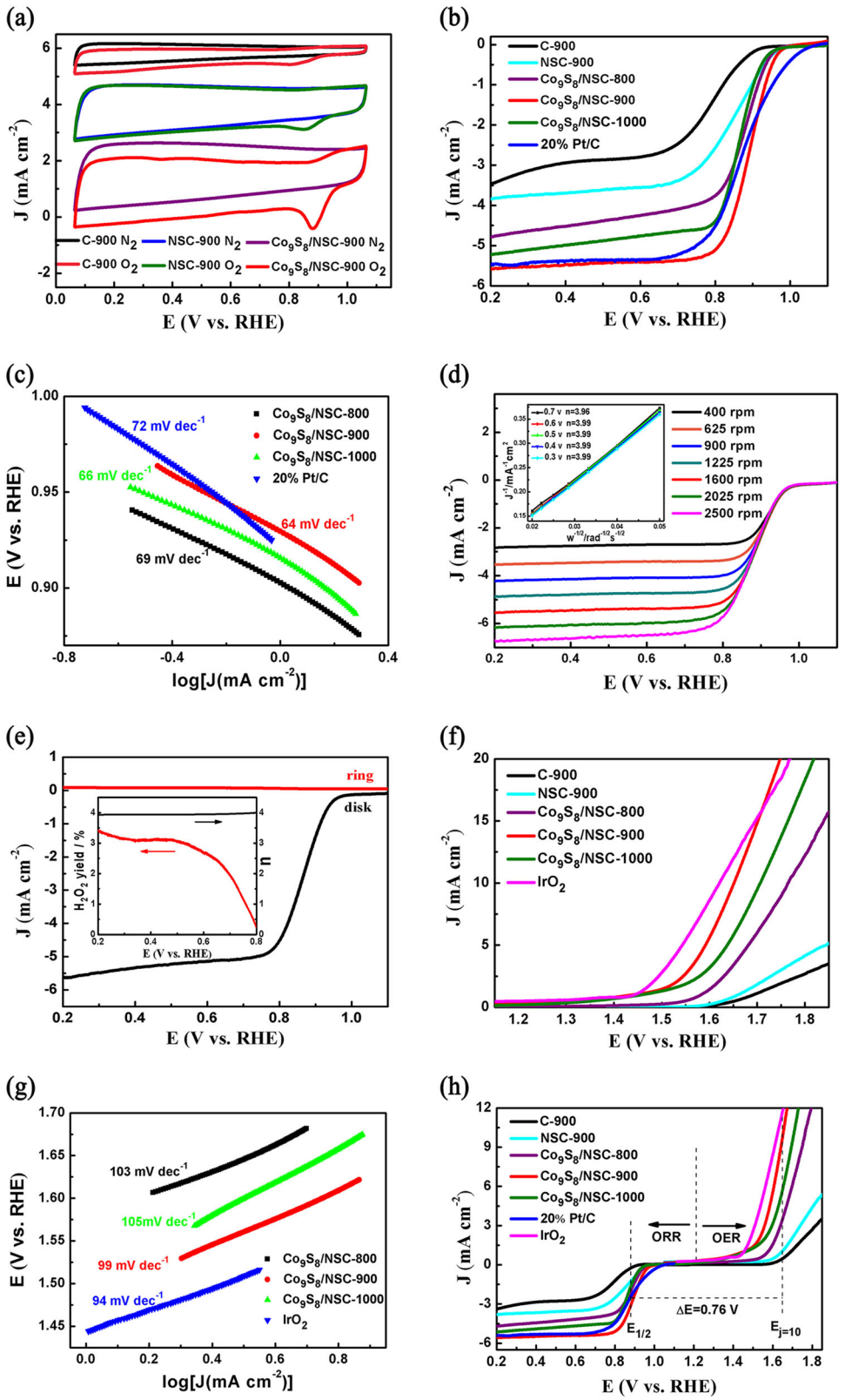

Fig. 6 (See legend on next page.)

(see figure on previous page)
Fig. 6 Electrochemical performance characterization for ORR and OER, **a** CVs of C-900, NSC-900 and Co_9S_8/NSC-900 in-situ composites in N_2 and O_2-saturated 0.1 M KOH. Scan rate: 20 mV s-1; **b** Steadystate LSVs on different catalysts at a rotating rate of 1600 rpm in O_2-saturated 0.1 M KOH; **c** Tafel plot of Co_9S_8/NSC-800, Co_9S_8/NSC-900, Co_9S_8/NSC-1000, and 20% Pt/C; **d** LSVs for the ORR/K-L plots of Co_9S_8/NSC-900 in-situ composites at different rotating rates; **e** peroxide yield and electron transfer numbers for Co_9S_8/NSC-900 obtained from RRDE voltammograms at a rotating rate of 1600 rpm in O_2- saturated 0.1 M KOH; **f** LSVs for the OER of Co_9S_8/NSC-900 in-situ composites in 0.1 M KOH at 1600 rpm for different catalysts (scan rate, 5 mV s-1; electrolyte in 0.1 M KOH; rotation speed, 1600 rpm); **g** Tafel plot of Co_9S_8/NSC-800, Co_9S_8/NSC-900, Co_9S_8/NSC-1000, and IrO_2; **h** the overall LSV curves of all samples in the whole ORR and OER region in 0.1 M KOH

Table 1 List of the ORR/OER catalytic properties of the Co_9S8/NSC-900 in situ composites and previously reported state-of-the-art catalysts in 0.1 M KOH

Catalyst	Electrolyte	ORR, E_{onset}/V (vs. RHE),	ORR, $E_{1/2}/V$ (vs. RHE)	J_L (mA cm^{-2})	OER, E_{onset}/V (vs. RHE)	OER, $E_{(j=10)}/V$ (vs. RHE)	$\Delta E = E_{(j=10)} - E_{1/2}/V$ (vs. RHE)	Ref.
Co_9S_8/NSC-900	0.1 M KOH	0.96	**0.88**	5.56	1.51	1.64	**0.76**	This work
20 wt% Pt/C	0.1 M KOH	1.00	0.86	5.51	N.A.	N.A.	N.A.	This work
IrO_2	0.1 M KOH	N.A.	N.A.	N.A.	1.46	1.62	N.A.	This work
CoZn-NC700	0.1 M KOH	0.98	0.84	4.93	1.52	1.63	0.89	[29]
Co_9S_8@SNCC	0.1 M KOH	0.85	0.75	5.23	–	1.56	0.81	[38]
CoNCF-1000-80	0.1 M KOH	0.92	0.82	5.03	1.63	1.66	0.84	[47]
NC@Co-NGC	0.1 M KOH	0.92	0.82	5.3	1.53	1.64	0.82	[49]
NPBC	0.1 M KOH	0.98	0.86	5.10	1.52	1.68	0.82	[50]
NiCo/PFC	0.1 M KOH	0.92	0.79	5.61	1.51	1.62	0.83	[52]
Co-N-GCI	0.1 M KOH	0.92	0.85	5.50	1.61	1.66	0.81	[58]
Fe@C-NG/NCNTs	0.1 M KOH	0.93	0.84	5.00	1.68	1.68	0.84	[59]

The bold value means the best performance in this item compared to the previously reported works list in the table.

(Figure S5f). These results directly indicated the superior stability of the Co_9S_8/NSC-900 catalyst in comparison with the commercial 20% Pt/C.

The OER catalytic activity is another very important performance parameter for the bifunctional oxygen electrocatalysts used in rechargeable Zn–air batteries. Therefore, the LSVs for the OER of the Co_9S_8/NSC-900 in situ composite catalysts were also measured in O_2-saturated 0.1 M KOH aqueous solution at 1600 rpm. Figure 6f shows that Co_9S_8/NSC-900 in situ composites exhibit a more positive onset potential (1.51 V vs. RHE) than that of C-900 (1.65 V vs. RHE), NSC-900 (1.64 V vs. RHE), Co_9S_8/NSC-800 (1.56 V vs. RHE), and Co_9S_8/NSC-1000 (1.54 V vs. RHE). Meanwhile, the Co_9S_8/NSC-900 in situ composites show a smaller overpotential (0.41 V vs. RHE) compared to that of Co_9S_8/NSC-800 (0.53 V vs. RHE), and Co_9S_8/NSC-1000 (0.47 V vs. RHE) at a current density of 10 mA cm^{-2}, approaching the value of commercial IrO_2 (0. 39 V vs. RHE) and indicated the good OER activity of Co_9S_8/NSC-900. The Tafel plots derived from LSV polarization curves further verify the good OER performance of Co_9S_8/NSC-900, as shown in Fig. 6g. The corresponding Tafel slope values for Co_9S_8/NSC-900, Co_9S_8/NSC-800, Co_9S_8/NSC-1000, and IrO_2 were calculated to be 99, 103, 105, and 94 mV dec^{-1}, respectively. Thus, apparently, Co_9S_8/NSC-900 also exhibits a close Tafel slope compared with that of the IrO_2 catalyst, also indicating the good OER activity of Co_9S_8/NSC-900. The OER stability of the Co_9S_8/NSC-900 in situ composites was further evaluated through 10,000 CV cycles at a high scan rate of 300 mV s^{-1} in O_2-saturated 0.1 M KOH between 1.1 and 1.8 V (vs. RHE). The observed overpotential in the polarization curve recorded after 10,000 cycles only shows a small decline of 27 mV (Figure S5g). In comparison, the commercial IrO_2 catalyst exhibited a larger attenuation of 41 mV after 10,000 cycles (Figure S5h). These results directly indicate the superior stability of the Co_9S_8/NSC-900 catalyst in the OER in comparison with the commercial IrO_2 catalyst.

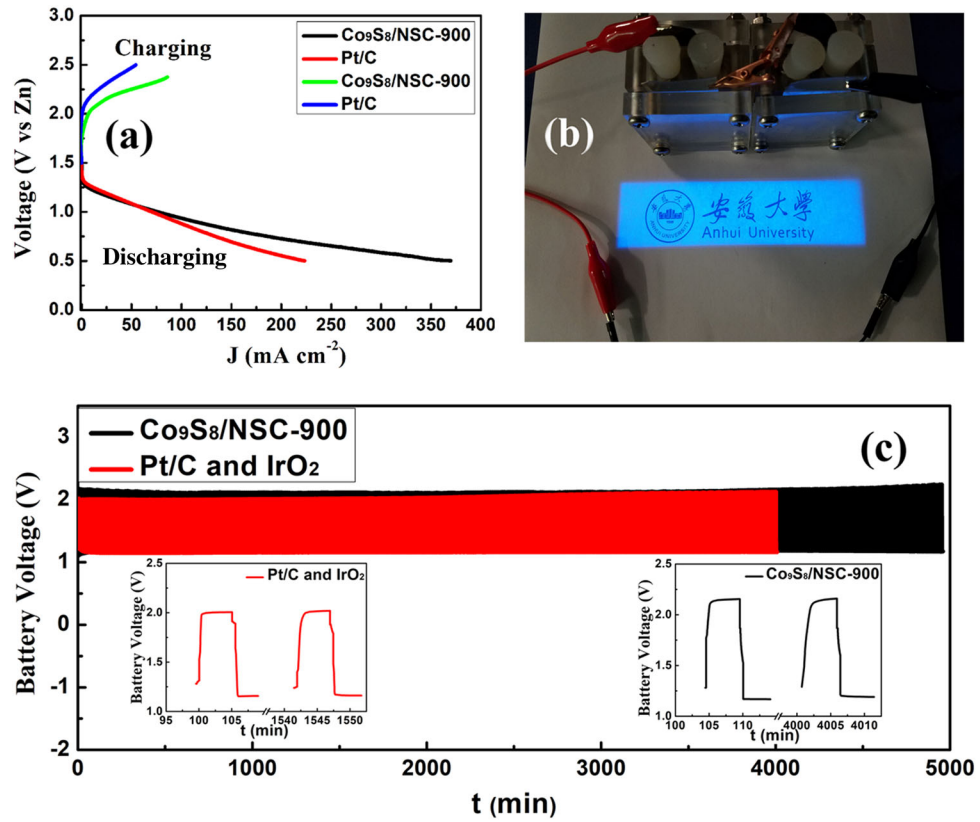

Fig. 7 Performance characterization of rechargeable Zn–air battery, **a** Charge and discharge polarization curves of the fabricated Zn-air battery; **b** Photograph of a electroluminescence panel powered by two Zn-air batteries with the Co_9S_8/NSC-900 based air electrode connected in series; **c** Galvanostatic discharge-charge cycling curves at 10 mA cm-2 of rechargeable Zn–air batteries with the Co_9S_8/NSC-900 and commercial Pt/C-IrO_2 catalyst based air electrode, respectively

To intuitively grasp the catalytic performance of bifunctional honeycomb-like Co_9S_8/NSC-900 in situ composites, the key parameters for evaluating the ORR/OER catalytic activity were compared to those of other currently reported state-of-the-art catalysts (Table 1). As shown Fig. 6h, it is obvious that the Co_9S_8/NSC-900 in situ composites exhibit excellent ORR/OER bifunctional catalytic activity with a small potential difference ($\Delta E = 0.76$ V) between the half-wave potential of the ORR and the potential of the OER at 10 mA cm^{-2}, which is usually used to estimate the performance of a bifunctional oxygen electrode catalyst[58–60]. We believe that the main reason for the excellent ORR/OER catalytic activity might be attributed to following reasons, First, the doping with the highly electronegative heteroatoms N and S can significantly increase the conductivity of the honeycomb-like carbon porous skeleton, which can further improve the poor conductivity of Co_9S_8 nanocatalysts through the strong interface coupling between the in situ embedded monodisperse Co_9S_8 nanoparticles and the outer carbon matrix, providing an advantageous channel for electron mobility. Second, the tendency of the monodisperse Co_9S_8 nanoparticles to aggregate during continuous work can be greatly relieved through the in situ embedding within the porous carbon skeleton. Moreover, the 3D interconnected porous network with high specific surface area can guarantee a large nanocatalyst loading amount, thus providing more active sites generated from the in situ embedded Co_9S_8 nanoparticles accessible to the electrolyte. Last but not the least, the 3D interconnected porous network is also beneficial for the mass transport of electrolyte ions and ORR/OER-related species during the catalytic process, allowing a rapid and sustained reaction.

Performance of rechargeable Zn–air battery

Finally, based on the excellent bifunctional oxygen catalytic activity (ORR/OER) of the as-prepared Co_9S_8/NSC-900 electrocatalyst, a two-electrode rechargeable zinc–air battery was fabricated. The custom-made zinc–air battery was assembled with a Zn plate serving as an anode, Co_9S_8/NSC-900 serving as the air–cathode catalyst, and a 6.0 M KOH solution containing 0.2 M Zn $(Ac)_2$ serving as an electrolyte. It is known that a minor overpotential region for the charge and discharge

potential is beneficial for the application of an electrocatalyst in rechargeable zinc–air batteries with high-performance. Figure 7a shows that the discharge/charge voltages of the Co_9S_8/NSC-900 bifunctional oxygen electrocatalyst at the current density of 50 mA cm^{-2} are 1.10/2.25 V, superior to the discharge/charge voltage of commercial Pt/C (1.09/2.47 V) at the same current density, indicating the superior performance of the fabricated rechargeable zinc–air battery based on Co_9S_8/NSC-900 eletrocatalyst. Notably, Co_9S_8/NSC-900 discharged better at the larger densities. In addition, the electroluminescence panel was successfully powered by two tandem Zn–air batteries based on the Co_9S_8/NSC-900 eletrocatalyst (Fig. 7b), directly indicating the great potential of our designed and prepared eletrocatalyst to be used for actual energy storage and conversion devices. The battery cycling test was further conducted to confirm the recharging ability of the fabricated Zn–air battery based on the Co_9S_8/NSC-900 eletrocatalyst. When cycled at a current density of 10 mA cm^{-2}, the battery fabricated on the Co_9S_8/NSC-900 eletrocatalyst exhibited considerably stable charge/discharge potentials at 2.14/1.18 V, respectively (Fig. 7c). The whole charging and discharging overpotential for Co_9S_8/NSC-900 was ~0.96 V, approaching that of the commercial Pt/C–IrO_2 composite catalyst (2.0/1.15 V, 0.85 V), corresponding to a high voltaic efficiency of 55.1%, comparable to that of the commercial Pt/C–IrO_2 composite catalyst (57.5%). However, after 4000 min, the polarization potential and current efficiency remained almost unchanged, indicating a better long-term cycling stability than that based on the commercial Pt/C–IrO_2 composite catalyst, for which the cycling stability tended to deteriorate after ~1500 min, as shown in Fig. 7c. All of the results indicated the superior competitive power of the honeycomb-structured porous Co_9S_8/NSC-900 in situ composites in terms of bifunctional catalytic activities, stabilities, and efficiency for applications in energy storage and conversion devices.

Conclusion

In this work, inspired by honeycombs in nature, a unique honeycomb-structured porous Co_9S_8/NSC hybrid bifunctional oxygen electrocatalyst was designed and fabricated with N, S-codoped honeycomb-structured carbon with high conductivity serving as the porous skeleton, within which were homogeneously in situ-embedded monodisperse Co_9S_8 nanoparticles (2–20 nm) serving as highly active catalysts providing more active sites. Thanks to the rational design of honeycomb-like porous hybrid structure and appropriate material selection, the as-fabricated honeycomb-structured porous Co_9S_8/NSC in situ composites not only exhibited higher catalytic activity but also better durability and methanol tolerance compared to that of the commercial Pt/C catalyst. In particular, the half-wave potential (0.88 V vs. RHE) clearly outperformed that of the commercial 20% Pt/C (0.86 V vs. RHE) catalyst in alkaline electrolyte. Furthermore, the Co_9S_8/NSC in situ composites also present good catalytic activity and stability for the OER in terms of a small overpotential (0.41 V vs. RHE at 10 mA cm^{-2}). Thus, a rechargeable Zn–air battery was further assembled based on the honeycomb-structured porous Co_9S_8/NSC in situ composites served as the air electrode with dual electrocatalytic activity, which exhibited a narrow discharge–charge voltage gap (0.96 V) with a high voltaic efficiency of 55.1% at 10 mA cm^{-2}, comparable to those of an assembled battery based on the commercial Pt/C–IrO_2 composite catalyst (0.85 V, 57.5%), and a better cycling stability over 4000 min than that of the commercial Pt/C–IrO_2 composite catalyst (~1500 min). Other distinctive features include scalable throughput and a simple, as well as cost-effective fabrication process, which jointly make our designed honeycomb-structured porous Co_9S_8/NSC-900 bifunctional eletrocatalyst with superior competitive power appropriate for applications in energy storage and conversion devices.

Acknowledgements
This work was financed by the National Key R&D Program of China (2017YFA0403600), the National Natural Science Foundation of China (11374013, 51672001, and 21401202), the Distinguished Youth Foundation of Anhui Province(1808085J10), and the International cooperation fund of Anhui Province (1704e1002209).

Conflict of interest
The authors declare that they have no conflict of interest.

Supplementary information is available for this paper at https://doi.org/10.1038/s41427-018-0063-0.

Received: 10 February 2018 Revised: 17 May 2018 Accepted: 27 May 2018.
Published online: 27 July 2018

References

1. Porter, N. S., Wu, H., Quan, Z. & Fang, J. Shape-control and electrocatalytic activity-enhancement of pt-based bimetallic nanocrystals. *Acc. Chem. Res.* **46**, 1867–1877 (2013).
2. Park, J., Park, M., Nam, G., Lee, J. S. & Cho, J. All-solid-state cable-type flexible zinc-air battery. *Adv. Mater.* **27**, 1396–1401 (2015).
3. Han, Y., Dong, X., Zhang, C. & Liu, S. Hierarchical porous carbon hollow-spheres as a high performance electrical double-layer capacitor material. *J. Power Sources* **211**, 92–96 (2012).
4. Ye, C. et al. A 3D hybrid of chemically coupled nickel sulfide and hollow carbon spheres for high performance lithium–sulfur batteries. *Adv. Funct. Mater.* **27**, 1702524 (2017).
5. Shen, K. et al. Ordered macro-microporous metal-organic framework single crystals. *Science* **359**, 206–210 (2018).
6. Murry, C. E. & Minh, H. N. Just a dream—or future reality? *Science* **324**, 48–49 (2009).
7. Davari, E. & Ivey, D. G. Bifunctional electrocatalysts for Zn-air batteries. *Sustain. Energy Fuels* **2**, 39–67 (2018).

8. He, D. S. et al. Ultrathin icosahedral Pt-enriched nanocage with excellent oxygen reduction reaction activity. *J. Am. Chem. Soc.* **138**, 1494–1497 (2016).
9. Ranjbar Sahraie, N., Paraknowitsch, J. P., Göbel, C., Thomas, A. & Strasser, P. Noble-metal-free electrocatalysts with enhanced ORR performance by task-specific functionalization of carbon using ionic liquid precursor systems. *J. Am. Chem. Soc.* **136**, 14486–14497 (2014).
10. Li, M., Bo, X., Zhang, Y., Han, C., Nsabimana, A. & Guo, L. Cobalt and nitrogen co-embedded onion-like mesoporous carbon vesicles as efficient catalysts for oxygen reduction reaction. *J. Mater. Chem. A* **2**, 11672 (2014).
11. Tian, J. et al. Three-dimensional porous supramolecular architecture from ultrathin g-C_3N_4 nanosheets and reduced graphene oxide: Solution self-assembly construction and application as a highly efficient metal-free electrocatalyst for oxygen reduction reaction. *ACS Appl. Mater. Interfaces* **6**, 1011–1017 (2014).
12. Huo, R., Jiang, W.-J., Xu, S., Zhang, F. & Hu, J.-S. Co/CoO/$CoFe_2O_4$/G nanocomposites derived from layered double hydroxides towards mass production of efficient Pt-free electrocatalysts for oxygen reduction reaction. *Nanoscale* **6**, 203–206 (2014).
13. Guo, C. et al. Engineering high-energy interfacial structures for high-performance oxygen-involving electrocatalysis. *Angew. Chem.-Int. Ed.* **56**, 8539–8543 (2017).
14. Masa, J. et al. Mn_xO_y/NC and Co_xO_y/NC nanoparticles embedded in a nitrogen-doped carbon matrix for high-performance bifunctional oxygen electrodes. *Angew. Chem.- Int. Ed.* **53**, 8508–8512 (2014).
15. Wang, M. et al. The role of iron nitrides in the Fe-N-C catalysis system towards the oxygen reduction reaction. *Nanoscale* **9**, 7641–7649 (2017).
16. Ma, T. Y., Ran, J., Dai, S., Jaroniec, M. & Qiao, S. Z. Phosphorus-doped graphitic carbon nitrides grown in situ on carbon-fiber paper: flexible and reversible oxygen electrodes. *Angew. Chem. - Int. Ed.* **54**, 4646–4650 (2015).
17. Hu, C. & Dai, L. Multifunctional carbon-based metal-free electrocatalysts for simultaneous oxygen reduction, oxygen evolution, and hydrogen evolution. *Adv. Mater.* **29**, 1604942 (2017).
18. Dai, L., Xue, Y., Qu, L., Choi, H. J. & Baek, J. B. Metal-free catalysts for oxygen reduction reaction. *Chem. Rev.* **115**, 4823–4892 (2015).
19. Choi, J.-Y. et al. Is the rapid initial performance loss of Fe/N/C non precious metal catalysts due to micropore flooding? *Energy Environ. Sci.* **10**, 296–305 (2017).
20. Zeng, S. et al. Crosslinked carbon nanotube aerogel films decorated with cobalt oxides for flexible rechargeable Zn-air batteries. *Small* **13**, 1700518 (2017).
21. Hu, H., Han, L., Yu, M., Wang, Z. & Lou, X. W. Metal-organic-framework-engaged formation of Co nanoparticle-embedded carbon@Co_9S_8 double-shelled nanocages for efficient oxygen reduction. *Energy Environ. Sci.* **9**, 107–111 (2016).
22. Zheng, Y. et al. Molecule-level g-C_3N_4 coordinated transition metals as a new class of electrocatalysts for oxygen electrode reactions. *J. Am. Chem. Soc.* **139**, 3336–3339 (2017).
23. Dou, S., Tao, L., Huo, J., Wang, S. & Dai, L. Etched and doped Co_9S_8/graphene hybrid for oxygen electrocatalysis. *Energy Environ. Sci.* **9**, 1320–1326 (2016).
24. Wang, J., Li, L., Chen, X., Lu, Y. & Yang, W. Monodisperse cobalt sulfides embedded within nitrogen-doped carbon nanoflakes: an efficient and stable electrocatalyst for the oxygen reduction reaction. *J. Mater. Chem. A* **4**, 11342–11350 (2016).
25. Zhong, H. et al. In situ anchoring of Co_9S_8 nanoparticles on N and S co-doped porous carbon tube as bifunctional oxygen electrocatalysts. *NPG Asia Mater.* **8**, e308 (2016).
26. Hou, Y. et al. Strongly coupled 3D hybrids of N-doped porous carbon nanosheet/CoNi alloy-encapsulated carbon nanotubes for enhanced electrocatalysis. *Small* **11**, 5940–5948 (2015).
27. Ai, W. et al. Nitrogen and sulfur codoped graphene: multifunctional electrode materials for high-performance LI-ion batteries and oxygen reduction reaction. *Adv. Mater.* **26**, 6186–6192 (2014).
28. Wu, G. et al. Carbon nanocomposite catalysts for oxygen reduction and evolution reactions: From nitrogen doping to transition-metal addition. *Nano Energy* **29**, 83–110 (2016).
29. Chen, B. et al. MO-Co@N-doped carbon (M = Zn or Co): vital roles of inactive Zn and highly efficient activity toward oxygen reduction/evolution reactions for rechargeable Zn-air battery. *Adv. Funct. Mater.* **27**, 1700795 (2017).
30. Duan, J., Chen, S., Dai, S. & Qiao, S. Z. Shape control of Mn_3O_4 nanoparticles on nitrogen-doped graphene for enhanced oxygen reduction activity. *Adv. Funct. Mater.* **24**, 2072–2078 (2014).
31. Li, J. et al. Direct transformation from graphitic C_3N_4 to nitrogen-doped graphene: an efficient metal-free electrocatalyst for oxygen reduction reaction. *ACS Appl. Mater. Interfaces* **7**, 19626–19634 (2015).
32. Yang, Z. et al. Sulfur-doped graphene as an efficient metal-free cathode catalyst for oxygen reduction. *ACS Nano* **6**, 205–211 (2012).
33. Yang, M. et al. Bifunctional MOF-derived carbon photonic crystal architectures for advanced Zn-air and Li-S batteries: highly exposed graphitic nitrogen matters. *Adv. Funct. Mater.* **27**, 1701971 (2017).
34. Cao, X. et al. Cobalt sulfide embedded in porous nitrogen-doped carbon as a bifunctional electrocatalyst for oxygen reduction and evolution reactions. *Electrochim. Acta* **191**, 776–783 (2016).
35. Liu, Y. et al. ZIF-derived graphene coated/Co_9S_8 nanoparticles embedded in nitrogen doped porous carbon polyhedrons as advanced catalysts for oxygen reduction reaction. *Int. J. Hydrogen Energy* **42**, 12978–12988 (2017).
36. Meng, C. et al. Atomically and electronically coupled Pt and CoO hybrid nanocatalysts for enhanced electrocatalytic performance. *Adv. Mater.* **29**, 1604607 (2017).
37. Li, Q. et al. Synthesis of mesoporous carbon spheres with a hierarchical pore structure for the electrochemical double-layer capacitor. *Carbon* **49**, 1248–1257 (2011).
38. Liu, S. et al. Containing Co-MOF derived Co_9S_8 @S,N-doped carbon materials as efficient oxygen electrocatalysts and supercapacitor electrode materials. *Inorg. Chem. Front.* **4**, 491–498 (2017).
39. Wang, X. D. et al. Preparation of spherical silica particles by Stöber process with high concentration of tetra-ethyl-orthosilicate. *J. Colloid Interface Sci.* **341**, 23–29 (2010).
40. Zhou, R., Zheng, Y., Jaroniec, M. & Qiao, S.-Z. Determination of the electron transfer number for the oxygen reduction reaction: from theory to experiment. *ACS Catal.* **6**, 4720–4728 (2016).
41. Pan, Y., Liu, Y. & Liu, C. Phase- and morphology-controlled synthesis of cobalt sulfide nanocrystals and comparison of their catalytic activities for hydrogen evolution. *Appl. Surf. Sci.* **357**, 1133–1140 (2015).
42. Feng, L. L. et al. Carbon-armored Co_9S_8 nanoparticles as all-pH efficient and durable H_2-evolving electrocatalysts. *ACS Appl. Mater. Interfaces* **7**, 980–988 (2015).
43. Wang, D., Fang, G., Xue, T., Ma, J. & Geng, G. A melt route for the synthesis of activated carbon derived from carton box for high performance symmetric supercapacitor applications. *J. Power Sources* **307**, 401–409 (2016).
44. Lv, H., Ji, G., Liu, W., Zhang, H. & Du, Y. Achieving hierarchical hollow carbon@Fe@Fe_3O_4 nanospheres with superior microwave absorption properties and lightweight features. *J. Mater. Chem. C.* **3**, 10232–10241 (2015).
45. Li, H. et al. Template synthesis of $CoSe_2$/Co_3Se_4 nanotubes: tuning of their crystal structures for photovoltaics and hydrogen evolution in alkaline medium. *J. Mater. Chem. A* **5**, 4513–4526 (2017).
46. Chen, B. et al. Cobalt sulfide/N, S codoped porous carbon core-shell nanocomposites as superior bifunctional electrocatalysts for oxygen reduction and evolution reactions. *Nanoscale* **7**, 20674–20684 (2015).
47. Jiang, H., Liu, Y., Li, W. & Li, J. Co nanoparticles confined in 3D nitrogen-doped porous carbon foams as bifunctional electrocatalysts for long-life rechargeable Zn-air batteries. *Small* **14**, 1703739 (2018).
48. Chen, Y. Z. et al. From bimetallic metal-organic framework to porous carbon: high surface area and multicomponent active dopants for excellent electrocatalysis. *Adv. Mater.* **27**, 5010–5016 (2015).
49. Liu, S. et al. Metal-organic-framework-derived hybrid carbon nanocages as a bifunctional electrocatalyst for oxygen reduction and evolution. *Adv. Mater.* **29**, 1700874 (2017).
50. Wang, Q. et al. Mass production of porous biocarbon self-doped by phosphorus and nitrogen for cost-effective zinc-air batteries. *Electrochim. Acta* **257**, 250–258 (2017).
51. Shen, L. et al. Formation of nickel cobalt sulfide ball-in-ball hollow spheres with enhanced electrochemical pseudocapacitive properties. *Nat. Commun.* **6**, 7694 (2015).
52. Fu, G. et al. Novel hydrogel-derived bifunctional oxygen electrocatalyst for rechargeable air cathodes. *Nano Lett.* **16**, 6516–6522 (2016).
53. Ganesan, P., Prabu, M., Sanetuntikul, J. & Shanmugam, S. Cobalt sulfide nanoparticles grown on nitrogen and sulfur codoped graphene oxide: an efficient electrocatalyst for oxygen reduction and evolution reactions. *ACS Catal.* **5**, 3625–3637 (2015).
54. Lai, L. et al. Exploration of the active center structure of nitrogen-doped graphene-based catalysts for oxygen reduction reaction. *Energy Environ. Sci.* **5**, 7936–7942 (2012).

55. Zhu, C. Z. et al. Self-assembled Fe-N-doped carbon nanotube aerogels with single-atom catalyst feature as high-efficiency oxygen reduction electrocatalysts. *Small* **13**, 1603407 (2017).
56. Lee, K. E. et al. Liquid crystal size selection of large-size graphene oxide for size-dependent N-doping and oxygen reduction catalysis. *ACS Nano* **8**, 9073–9080 (2014).
57. Wu, Z. Y. et al. Co/Co_3O_4/C-N, a novel nanostructure and excellent catalytic system for the oxygen reduction reaction. *Nano Energy* **8**, 118–125 (2014).
58. Qiao, X. et al. Cobalt and nitrogen codoped graphene with inserted carbon nanospheres as an efficient bifunctional electrocatalyst for oxygen reduction and evolution. *ACS Sustain. Chem. Eng.* **4**, 4131–4136 (2016).
59. Lei, Y. P. et al. Fe/Fe_3C@C nanoparticles encapsulated in N-doped graphene-CNTs framework as an efficient bifunctional oxygen electrocatalyst for robust rechargeable Zn-air batteries. *J. Mater. Chem. A* **6**, 516–526 (2018).
60. Xu, X., Song, F. & Hu, X. A nickel iron diselenide-derived efficient oxygen-evolution catalyst. *Nat. Commun.* **7**, 1–7 (2016).